Adaptive hard and tough mechanical response in single-crystal B1 VN_x ceramics via control of anion vacancies

A.B. Mei,[1] H. Kindlund,[2] E. Broitman,[3,4] L. Hultman,[4] I. Petrov,[4,5] J.E. Greene,[4,5,6]
D.G. Sangiovanni[4,7*]

[1]Department of Materials Science and Engineering, Cornell University, Ithaca, NY, 14853, USA

[2]Department of Materials Science and Engineering, University of California,
Los Angeles, CA 90095, USA

[3]SKF, Research & Technology Development, 3992AE Houten, Netherlands

[4]Department of Physics, Chemistry and Biology (IFM) Linköping University,
SE-581 83, Linköping, Sweden

[5]Department of Materials Science and the Materials Research Laboratory University of Illinois,
104 South Goodwin, Urbana, IL 61801, USA

[6]Department of Materials Science, National Taiwan University of Science and Technology,
Taipei 10607, Taiwan

[7]Interdisciplinary Centre for Advanced Materials Simulation (ICAMS),
Ruhr-Universität Bochum, D-44780 Bochum, Germany

High hardness and toughness are generally considered mutually exclusive properties for single-crystal ceramics. Combining experiments and *ab initio* molecular dynamics (AIMD) atomistic simulations at room temperature, we demonstrate that both the hardness and toughness of single-crystal NaCl-structure VN_x/MgO(001) thin films are simultaneously enhanced through the incorporation of anion vacancies. Nanoindentation results show that $VN_{0.8}$, here considered as representative understoichiometric VN_x system, is ≈20% harder, as well as more resistant to fracture than stoichiometric VN samples. AIMD modeling of VN and $VN_{0.8}$ supercells subjected to [001] and [110] elongation reveal that the tensile strengths of the two materials are similar. Nevertheless, while the stoichiometric VN phase cleaves in a brittle manner at tensile yield points, the understoichiometric compound activates transformation-toughening mechanisms that dissipate accumulated stresses. AIMD simulations also show that $VN_{0.8}$ exhibits an initially greater resistance to both $\{110\}\langle1\bar{1}0\rangle$ and $\{111\}\langle1\bar{1}0\rangle$ shear deformation than VN. However, for progressively increasing shear strains, the $VN_{0.8}$ mechanical behavior gradually evolves from harder to more ductile than VN. The transition is mediated by anion vacancies, which facilitate $\{110\}\langle1\bar{1}0\rangle$ and $\{111\}\langle1\bar{1}0\rangle$ lattice slip by reducing activation shear stresses by as much as 35%. Electronic-structure analyses show that the two-regime hard/tough mechanical response of $VN_{0.8}$ primarily stems from its intrinsic ability to transfer d electrons between 2nd-neighbor and 4th-neighbor (i.e., across vacancy sites) V–V metallic states. Our work offers a route for electronic-structure design of hard materials in which a plastic mechanical response is triggered with loading.
*Corresponding author: davide.sangiovanni@liu.se

1. Introduction

Brittle fracture in ceramics is primarily caused by the limited ability of these materials to dissipate mechanical stresses ahead of a growing crack [1, 2]. Accordingly, a strategy adopted to mitigate brittleness involves enhancing hardness while simultaneously hindering or deflecting crack propagation. This is commonly achieved through grain-boundary [3] and nanostructure engineering [4, 5]. However, recent experimental results [6-9] demonstrated that single-crystal NaCl-structure (B1) pseudobinary $V_{0.5}Mo_{0.5}N$ transition-metal (TM) nitride ceramics are intrinsically *both* hard (~20 GPa) and ductile. This surprising finding confutes the commonly accepted assumption that excellent ductility and high strength (well-correlated to hardness in solids [10, 11]) are mutually-exclusive material properties [12, 13]. Experiments have also proven that single-crystal B1 $V_{0.5}Mo_{0.5}N_x$ solid solutions become much harder (from 17 to 26 GPa) when the concentration of anion vacancies increases up to 45% [7].

Previous experimental results show that the hardness (H) of B1 Group-VB (i.e. V, Nb, and Ta) nitrides and carbides is enhanced by anion vacancies [14-17], consistent with H vs. x trends in $V_{0.5}Mo_{0.5}N_x$ [7-9]. Nonetheless, although understoichiometric $V_{0.5}Mo_{0.5}N_x$ is considerably less prone to crack than single-crystal B1 TiN and B1 VN, it is more susceptible to fracturing than stoichiometric $V_{0.5}Mo_{0.5}N$ [7]. This raises the question of whether hardness and ductility can be enhanced at the same time by controlling the metal/non-metal compositional ratio in refractory carbonitrides.

In this work, we combine experiments and *ab initio* molecular dynamics (AIMD) atomistic simulations to demonstrate that control of the N/V stoichiometry in VN_x allows simultaneously enhancing hardness, ductility, and toughness. The experiments are conducted on high-quality single-crystal B1 VN_x deposited epitaxially on MgO(001) with nitrogen-to-vanadium ratios x spanning 0.8 – 1.0 [18-20]. Nanoindentation testing show that the unusual combination of remarkable mechanical properties in understoichiometric $VN_{0.8}$ – in preliminary tests, $VN_{0.8}$ exhibits the best performance among all investigated VN_x systems – unambiguously originates

from anion vacancies. AIMD simulations of VN and $VN_{0.8}$ subjected to tensile deformation (up to fracture) and uniform shearing (up to lattice slip) at 300 K are used to unravel key atomistic and electronic mechanisms responsible for the superior mechanical behavior induced by vacancies. The results provide unprecedented insights for simultaneously enhancing hardness, ductility, and toughness in single-crystal TM carbonitride ceramics simply by controlling the lattice stoichiometry.

2. Methods

2.1. Experimental. The B1 structure of VN_x compounds has a large single-phase field that can accommodate compositional variations $0.7 < x \leq 1$, possible through incorporation of anion vacancies. VN_x/MgO(001) thin films with x spanning from 0.8 to 1.0 are grown to a thickness of 300 nm under 20 mTorr mixed N_2/Ar atmospheres in an ultra-high-vacuum magnetically-unbalanced reactive magnetron sputter-deposition system. Anion sublattice occupancy is controlled by varying the N_2 gas fraction between 0.1 and 1.0 and the growth temperature between 430 and 540 °C [19]. Rutherford backscattering spectroscopy is employed to determined nitrogen-to-vanadium ratios to an accuracy of ±0.05. MgO is selected as substrate material because it is isostructural with VN and exhibits a sufficient film/substrate lattice mismatch (0.9%) to enable film relaxation, a necessity for the investigation of intrinsic properties.

VN_x(001) hardness and Young's moduli values as a function of x are quantified [21, 22] via nanoindentation experiments performed on 300-nm-thick films in a Hysitron TI950 Triboindenter using a sharp Berkovich 142.3° diamond probe (tip radius ~150 nm) calibrated to an epitaxial TiN/MgO(001) sample. Nine indentations, arranged in a 3×3 pattern with indents separated by 10 µm, are made in each sample with a maximum tip penetration limited to 10% of the film thickness, which was verified to avoid spurious substrate effects on measured hardness values. The fracture toughness of VN_x samples is assessed via nanoindentation using a cube-corner diamond probe, which is sharper than a Berkovich tip and thus results in higher contact stresses

[23]. We performed two different tests: indentations at constant depths of 400 nm (which exceed the film thickness by 100 nm) and indentations as a function of penetration depth between 25 and 400 nm, at steps of 25 nm. At least 9 cube-corner indentations with constant depths of 400 nm were performed on each sample. The massive deformation induced in the films allows us to demonstrate the completely different mechanical behavior of stoichiometric VN (brittle) vs. understoichiometric $VN_{0.8}$ (supertough).

That compositional variations in understoichiometric VN_x are accommodated through anion vacancies is concluded based on the evolution of VN_x relaxed lattice parameters a_0 and mass densities ρ as a function of x. $a_0(x)$ values determined from x-ray diffraction (XRD) high-resolution reciprocal-space-maps decrease from 0.4134 nm (x = 1.0) to 0.4087 nm (x = 0.8) (details given in Ref. [19]) – a trend which is accurately described with first-principles density-functional theory (DFT) results obtained as a function of nitrogen vacancy concentrations [19]. VN_x/MgO(001) mass densities, obtained from x-ray reflectivity scans as well as Rutherford backscattering spectroscopy combined with film thickness measurements [20], decrease from 6.06 (x = 1.0) to 5.98 $g \cdot cm_{-3}$ (x = 0.76) [20]. $VN_{0.8}$ is expected to have a mass density of ≈ 6.0 $g \cdot cm_{-3}$, in close agreement with the experimentally determined value; V interstitials and V_N antisite substitutions would generate larger ρ values of 7.4 and 6.6 $g \cdot cm_{-3}$, respectively.

2.2. Modeling. Tensile and shear mechanical testing of VN_x systems are modelled using density-functional *ab initio* molecular dynamics [24] simulations at room temperature.

Tensile-testing simulations enable the evaluation of ideal tensile strength γ_T and toughness U_T for different strain directions. Deformation is applied orthogonal to (001) and (110) crystal surfaces, for which the energy of formation is lowest in B1-structure ceramics [25]. In AIMD modeling, γ_T corresponds to the maximum σ_{zz} stress reached during elongation, whereas U_T is calculated as the area that underlies the full stress/strain curve. Shear-deformation modeling is used to determine the resistance to change of shape of the materials, which is well-correlated with their hardness [26-28]. In addition, these simulations shed light on the mechanisms that govern the

activity of $\{110\}\langle1\bar{1}0\rangle$ and $\{111\}\langle1\bar{1}0\rangle$ slip systems, typically operative in B1-structure nitrides and carbides at room and/or elevated temperatures [29-31].

AIMD simulations are carried out with VASP [32] implemented with the projector augmented-wave method [33]. The Perdew-Burke-Ernzerhof (PBE) electronic exchange and correlation approximation [34], Γ-point sampling of the Brillouin zone, and planewave cutoff energies of 300 eV are used in all simulations. The ionic equations of motion are integrated at timesteps of 1 fs, using 10_{-5} eV/supercell convergence criteria for the total energy during both system equilibration and mechanical testing. Prior to modeling tensile and shear deformation, the supercell equilibrium structural parameters are determined via NPT simulations at 300 K using the Parrinello-Rahman barostat [35] and the Langevin thermostat. Thus, NVT sampling of the configurational space is used to equilibrate the unstrained structures for 5 additional ps using the Nose-Hoover thermostat. In these simulations, it is ensured that the time-averaged $|\sigma_{xx}|$, $|\sigma_{yy}|$, and $|\sigma_{zz}|$ stress components are $\lesssim 0.5$ GPa.

Our model supercells are oriented in a convenient manner for investigating the response of VN and $VN_{0.8}$ to tensile and shear deformation along different directions. Simulation boxes with [001] and [110] vertical (z) orientation are used to probe the dynamics of [001] and [110] tensile elongation, respectively. The supercells employed for $\{110\}\langle1\bar{1}0\rangle$ and $\{111\}\langle1\bar{1}0\rangle$ shear deformation (up to the activation of lattice slip) have the lateral (x) axis parallel to a Burgers vector direction $\langle1\bar{1}0\rangle$ and the vertical (z) axis orthogonal to a slip plane, i.e. $\{110\}$ or $\{111\}$. VN and $VN_{0.8}$ supercells with vertical [h k l] orientation are denoted below as VN_x(h k l).

Tensile testing is modeled for VN_x(001) and VN_x(110) supercells with 768 lattice positions (24 layers orthogonal to the strain direction; 32 sites per layer), following the procedure of Ref. [36, 37]. Briefly, at each δ_{zz} strain step (1% of the supercell vertical size), the systems are first coupled to an isokinetic, and then to a Nosé-Hoover, thermostat. The thermostat temperature is set to 300 K, for a total equilibration time of 3 ps. The structures are progressively elongated until they reach their fracture points. VN and $VN_{0.8}$ simulation boxes used for shear deformation are formed

of 576 lattice sites (24 layers parallel to the slip plane; 24 atomic positions per layer). The cells are equilibrated and sequentially deformed (shear strain steps $\delta_{xz}=0.02$), with procedure analogous to that used for tensile testing. In all $VN_{0.8}$ supercells, the vacancy distribution on the anion sublattice yields negligible degrees of short-range ordering, which is consistent with experimental analysis [19].

Average tensile σ_{zz} and shear σ_{xz} stresses are determined as a function of strain from 500 equilibrated AIMD configurations. We note that, while in previous *static* first-principles stress/strain calculations thermal disorder was mimicked by introducing arbitrary atomic displacements [27, 38], our simulations explicitly include temperature effects, thus providing a realistic description of phase transformations and non-linear elastic effects. The approach is particularly important for modeling crystal structures that are dynamically-stabilized by lattice vibrations, including B1 VN [39].

The simulation results are visualized using the VMD software [40]. Electron-transfer and energy-resolved electron-density maps are calculated for atomic configurations directly extracted from AIMD simulations at 300 K. Electron transfer is obtained by subtracting non-interacting atomic charge densities from the self-consistent electron density of the entire crystal. The electron densities in next-nearest-neighbor d-t_{2g} and 4$_{th}$-neighbor (across-vacancy) d-e_g metallic V states are visualized by resolving the total charge density into the energy intervals [-2 – 0 eV] and [-3 – -2 eV], respectively, where 0 corresponds to the Fermi level (E_F).

3. Results and discussion

3.1. Characterization and mechanical properties of VN_x films. Fig. 1a shows a typical XRD ω-2θ scan acquired using Cu $K_{\alpha 1}$ radiation (wavelength λ = 0.154056 nm) from an understoichiometric $VN_{0.8}$/MgO(001) layer. Only four peaks are observed: MgO 002 and 004 at 2θ = 42.8° and 94.0° and $VN_{0.8}$ 002 and 004 at 2θ = 43.9° and 96.8°. The absence of additional reflections, together with glancing angle and pole-figure scans (not shown), establish that VN_x(001)

layers are NaCl-structure single-crystal films epitaxially oriented cube-on-cube relative to their MgO(001) substrate, $(001)_{VNx} \parallel (001)_{MgO}$ and $[100]_{VNx} \parallel [100]_{MgO}$. These findings are confirmed by high-resolution cross-sectional transmission electron microscopy (HR-XTEM) results, including the micrograph shown in **Fig. 1b**.

In our single-crystal B1 VN_x(001) samples, understoichiometry is accommodated by vacancies on the anion sublattice [19]. Nanoindentation testing demonstrates that $VN_{0.8}$ is approximately 20% harder than VN ($H_{VN0.8} = 17.1\pm0.8$ vs. $H_{VN} = 14.0\pm0.8$ GPa). This finding is consistent with previous experimental results, which have shown that the hardness of B1 Group-VB nitrides, including VN_x, increases with a N content that decreases from 100 to ≈80% [14-17]. The increased hardness of $VN_{0.8}$ is attributed to reduced dislocation mobility, which is also observed indirectly through the incomplete strain relaxation (92%) of VN_x layers with x ≥ 0.05 vs. $0 \le x \le 0.05$ (97% nitrogen) [19]. Thus, nitrogen vacancies obstruct dislocation glide (at least for relatively low loads; see the results of AIMD shear deformation below) resulting in higher hardness. As discussed in conjunction with AIMD-calculated elastic constants and moduli (see **Sec. 3.2** below), $VN_{0.8}$ exhibits *greater* shear elastic stiffness, but *lower* Young's moduli than stoichiometric VN.

Mechanical testing of single-crystal films demonstrates that $VN_{0.8}$ is not only harder, but also tougher than the stoichiometric compound. Vacancy-induced toughening in understoichiometric $VN_{0.8}$ layers is experimentally demonstrated by analyzing nanoindentation load-displacement curves (**Fig. 2**) and assessing indentation-induced fracturing using scanning-electron microscopy (SEM) in **Fig. 3**. Load-displacement curves L(d) are generated by indenting VN_x/MgO(001) layers with x = 1.0 and 0.8 using a Berkovich diamond tip. For shallow indents (d < 10 nm), L increases as $d^{3/2}$, indicating that deformation in this region is purely elastic [41]. Indeed, SEM imaging shows that retracting the tip while operating in this regime leaves no impression on the sample surface. For deeper indents (d>10 nm), a striking difference is observed by varying the vacancy concentration. For stoichiometric VN, plastic deformation is indicated by pop-ins –

stochastically occurring displacement discontinuities [41, 42] – which reflect catastrophic mechanical failures on mesoscopic scales, including crack nucleation [43-45] and dislocation avalanches [46]. In contrast, nanoindentation load-displacement curves for understoichiometric $VN_{0.8}$ layers never exhibit pop-ins. Instead, L(d) gradually evolves into the elastoplastic regime through a series of small incremental displacements, suggesting that indentation stresses are continuously curbed below pop-in thresholds via the constant emission of dislocations.

Fig. 3a-b show representative SEM images in plan-view of 400-nm-deep indents (extending 100 nm into the MgO(001) substrate). Cube-corner nanoindentation results at constant penetrations of 400 nm demonstrate that $VN_{0.8}$ is considerably more resistant to fracture than VN. Indents into stoichiometric VN layers, **Fig. 3a**, exhibit 0.5-µm-long cracks propagating along [–110] directions. In contrast, understoichiometric $VN_{0.8}$ films *never* fracture. The absence of cracks in $VN_{0.8}$ layers is consistent with the continuous nanoindentation load-displacement curves observed for these samples and demonstrates their enhanced toughness. The integrity of the samples and absence of delamination at the film/substrate interface is assessed via cross-sectional SEM. A vertical section through an indentation site in stoichiometric VN/MgO(001), obtained with a focused Ga_+ ion beam in an FEI DualBeam 235 instrument, is presented in **Fig. 3c**. The indentation is triangular with a 0.5-µm-wide base. The tip of the indent lies 360 nm below the original film surface, indicating that 40 nm of the 400-nm-deep indent recovered elastically. The deformed VN/MgO(001) interface is 100 nm below the original interface. Despite the depth of the deformation, conformal contact is maintained along the entire film/substrate interface, indicating robust layer adhesion. Material pile-up around the indent occurs within 0.5 µm of indentation edges and rises 40 nm above the original surface.

Scanning probe microscopy (SPM) height isointensity contour maps show that plastic flow in indented VN samples occurs in the shape of a cross (**Fig. 3d**). Cube-corner indentation produces pronounced material pile-up (red areas in **Fig. 3d**) along ⟨110⟩ directions and less pile-up along ⟨100⟩. Mounds near the faces of the indentation triangle, where stress is concentrated, have heights

(≈50 nm) which are more than twice those (≈20 nm) of hillocks near the vertices of the indentation triangle (**Fig. 3d**). Azimuthal rotations of the indentor with respect to the orientations shown in **Fig. 3**, changes relative mound heights, but has negligible effects on the pattern shape, in agreement with finite element models [47]. Pile-up patterns on $VN_{0.8}(001)$ have similar shapes but exhibit smaller mounds, consistent with their higher hardness. The higher degree of material pile-up observed for VN is also reflected in a lower elastic recovery of these films. Using all the collected load-displacement data – 12 load/unload curves for each sample (not shown) – we estimate an elastic recovery of 42±1% for VN and 55±1% for $VN_{0.8}$. We note, however, that the value of elastic recovery calculated for VN is reduced by the fracturing (large pop-ins) of the films during loading (**Fig. 2a**).

The analysis of the residual stresses present in VN_x films is further in favor of our vacancy-induced toughening argument. At room temperature, the stoichiometric VN films have an in-plane residual compressive stress of -0.77 GPa. Although these compressive stresses should contribute to close the cracks upon unloading, the cracks remain visible after cube-corner nanoindentation of VN films. Conversely, the understoichiometric films have an in-plane residual tensile stress of +0.92 GPa. The fact that $VN_{0.8}$ films never crack despite of the presence of residual tensile stresses (which should favor crack formation) is a further proof of the excellent toughness of $VN_{0.8}$.

3.2. AIMD evaluation of VN_x mechanical properties at room temperature. AIMD modeling is used to evaluate intrinsic mechanical properties of B1 VN_x single crystals, and identify atomistic and electronic mechanisms responsible for the enhanced toughness and hardness of $VN_{0.8}$. Despite the fact that nanoindentation mainly produces compressive stresses in VN_x samples, the regions of the films that surround the nanoindenter edges are subjected to severe tensile stresses. Indeed, brittle nitrides crack in proximity of nanoindender edges and corners (see **Fig. 3a** for VN and figure 3(c,d) in Ref. [6] for $VN_{0.89}$ and $TiN_{0.96}$). Accordingly, AIMD tensile testing is useful to assess the inherent materials' resistance to brittle fracture.

The stress/strain curves determined for supercells subjected to [001] elongation (**Fig. 4a)** show that VN(001) and $VN_{0.8}(001)$ have ideal strengths (maximum stresses withstood during deformation) $\gamma_{TVN(001)}=36$ GPa and $\gamma_{TVN_{0.8}(001)}=32$ GPa. Strain along the [110] axis yields $\gamma_{TVN(110)}=46$ GPa and $\gamma_{TVN_{0.8}(110)}=42$ GPa, **Fig. 4b**. Hence, AIMD results show that the ideal tensile strength γ_T of $VN_{0.8}$ is within $\approx 10\%$ that of stoichiometric VN. However, $VN_{0.8}$ exhibits a much higher toughness and resistance to fracture than VN, with the most remarkable differences observed for [001]-strained compounds (**Fig. 4a**).

At an elongation of 14%, VN(001) cleaves on the (001) plane by sudden and essentially simultaneous breakage of V–N bonds parallel to the loading direction (**Figs. 5a and 4a**). In contrast, $VN_{0.8}(001)$ resists fracture up to an elongation of 30% (**Figs. 5b and 4a**). The crack develops between (001) lattice layers characterized by a relatively *low* concentration of anion vacancies. In addition, $VN_{0.8}$ displays a total tensile toughness [48] which is approximately twice that of VN. The simulations reveal that the considerably enhanced resistance to fracture of $VN_{0.8}$ is due to a transformation toughening mechanism, characterized by buckling of (001) atomic planes, activated by extreme tensile stress (**Fig. 5b**). Analogous to the results obtained for (001) supercells, $VN_{0.8}(110)$ also displays larger toughness than VN(110) (**Fig. 4b**) due to changes in bonding geometry activated at high tensile loading (AIMD snapshots not shown). The progressive transformation in the bonding network allows $VN_{0.8}$ to prevent stress build up, thereby hindering crack nucleation and actively toughening the material. The mechanism is similar to the one observed during AIMD mechanical testing [36] of hard and ductile B1 $V_{0.5}Mo_{0.5}N_x$ alloys [7]. We note that, within the supercell model considered here, the structural transformations identified in $VN_{0.8}$ compounds are fully reversible upon relaxation; after cleavage on (001) and (110) planes, $VN_{0.8}$ recovers the B1 structure.

As demonstrated by our nanoindentation tests, single-crystal B1 $VN_{0.8}$ samples $(H_{VN_{0.8}}=17.1\pm0.8$ GPa) are harder than stoichiometric films $(H_{VN}=14.0\pm0.8$ GPa). Detailed understanding of vacancy-induced hardening in VN_x single crystals would require the challenging

determination of representative dislocation-core structures – with their densities and nucleation mechanisms – as well as the kinetics of dislocation motion and dislocation/dislocation interactions [49-53]. Nevertheless, *ab initio* and experimental studies show that the trends in hardness of B1 TM nitrides and carbides are well correlated with their trends in shear elastic moduli [26, 28, 54, 55]. The fact that the hardness benefits from increased shear resistance is consistent with the results our experiments and AIMD simulations (see below).

Fig. 6 illustrates the shear stress σ_{xz} calculated for VN and $VN_{0.8}$ crystals subjected to $[1\bar{1}0]$ shearing of (110) and (111) crystallographic planes. The peculiar upward bending of σ_{xz} vs. strain δ_{xz} curves observed for small ($\delta_{xz} < 0.1$) shear deformations of VN(110) and VN(111) (**Fig. 6a-b**) is due to the large third-order elasticity of VN [56] (as elaborated in the following paragraphs). Conversely, the dependences of shear stresses σ_{xz} in understoichiometric $VN_{0.8}(110)$ and $VN_{0.8}(111)$ are quasilinear for $\delta_{xz} < 0.1$ (**Fig. 6a-b**). The calculated σ_{xz} values demonstrate that, within the elastic-response regime, $VN_{0.8}$ is more resistant to both $\{110\}\langle 1\bar{1}0\rangle$ and $\{111\}\langle 1\bar{1}0\rangle$ shear deformation than VN (note in **Fig. 6a-b** that $\sigma_{xzVN0.8} > \sigma_{xzVN}$ for $\delta_{xz} < 0.09$). Hence, $VN_{0.8}$ exhibits an *initially harder* response to change of shape than VN.

To elucidate the differences in measured hardness values, it is worth to closely analyze the elastic responses to deformation of B1 VN_x crystals. **Table 2** summarizes the results of the elastic constants and moduli evaluated by AIMD mechanical testing. The stiffnesses C_{11}, G_{110}, and G_{111u} – calculated from the slopes (linear regression for $\leq$2% deformation) of stress/strain curves presented in **Figs. 4a, 6a, and 6b**, respectively – quantify the *actual* elastic resistances of B1 VN_x crystals to $\langle 001\rangle$ uniaxial tension, $\{110\}\langle 1\bar{1}0\rangle$ and $\{111\}\langle 1\bar{1}0\rangle$ shearing at room temperature. **Table 2** also lists *effective* average elastic constants $\widetilde{C}_{11}$, $\widetilde{C}_{12}$, and $\widetilde{C}_{44}$ obtained by minimizing the least-square differences between the stress components extracted during AIMD simulations and those predicted according to the linear elastic theory approximation [57]. The differences between *actual* and *effective* elastic properties are indicative of the magnitude of nonlinear elastic effects. Indeed,

an ideal linear elastic response would yield essentially the same elastic constant values irrespectively of the choice of the strain tensor used for the calculation [56]. That also implies validity of the equivalences $\widetilde{C}_{ij} \equiv C_{ij}$ and that *actual* shear stiffnesses are accurately evaluated using the relations $G_{110} \equiv \widetilde{G}_{110} \equiv (C_{11}-C_{12})/2$ and $G_{111u} \equiv \widetilde{G}_{111u} \equiv (C_{11}-C_{12}+C_{44})/3$ [58, 59].

The *effective* average elastic properties $\widetilde{C}_{ij}$ determined for VN and VN$_{0.8}$ crystals are consistent with the range of values reported by acoustic waves measurements and DFT calculations at 0 K [18, 85-94] (see **Table 2**, [60, 61]). All $\widetilde{G}_{hkl}$ values are calculated as linear combinations of *effective* elastic constants (see end of previous paragraph). However, due to strong nonlinear elastic effects [56], the *actual* shear stiffnesses G_{110}^{VN} (116 GPa) and G_{111u}^{VN} (94 GPa) obtained via AIMD shear deformations of stoichiometric VN are $\approx 35\%$–50% *smaller* than $\widetilde{G}_{110}^{VN}$ (172 GPa) and $\widetilde{G}_{111u}^{VN}$ (193 GPa). Oppositely, the *actual* shear resistances of the understoichiometric compound ($G_{110}^{VN_{0.8}}$=205 GPa and $G_{111u}^{VN_{0.8}}$=190 GPa) are 20–25% larger than $\widetilde{G}_{hkl}^{VN_{0.8}}$ values (**Table 2**).

Nonlinear elastic effects are characteristic for anharmonic materials, as B1 VN [62], which are dynamically stabilized by lattice vibrations at finite temperatures [39, 63]. In the case of $\{110\}\langle 1\bar{1}0\rangle$ shear deformation, the initial upward curvature of the stress/strain dependence of VN (**Fig. 6a**) can be rationalized as a deformation-induced softening of transversal acoustic phonon modes. The $\{110\}\langle 1\bar{1}0\rangle$ shear deformation effectively corresponds to a pure tetragonal distortion of the cubic lattice (see illustration in figure 4 of [27]). The distortion is energetically facilitated by the B1→tetragonal VN transformation, which is a martensitic transition caused by phonon instabilities of the cubic lattice below 250 K (see schematic representation in figure 5 of [64], and results of electron and x-ray diffraction in figures 6 and 7 of [39]). On the contrary, experimental results indicate that an anion vacancy concentration of 3% thermodynamically stabilizes the B1 structure of VN$_x$ at cryogenic temperatures [63].

We propose that the greater shear elastic stiffnesses of VN$_{0.8}$ explain its experimentally-measured higher hardness in relation to VN. In addition to being harder than VN, the

understoichiometric compound exhibits the remarkable capability to adapt its mechanical response to the loading condition. As the shear strain increases beyond ≈9%, VN$_{0.8}$ becomes progressively more compliant to change of shape. This facilitates plastic deformation in VN$_{0.8}$, as evidenced by the smaller ideal shear strengths γ_s and strains δ_s required to activate $\{110\}\langle 1\bar{1}0\rangle$ and $\{111\}\langle 1\bar{1}0\rangle$ slip in VN$_{0.8}$ vs. VN (**Fig. 6 and Table 1**).

Although VN$_{0.8}$ displays *higher* hardness and shear elastic stiffnesses than VN, both AIMD results and nanoindentation measurements show that VN$_{0.8}$ has a *smaller* Young's modulus than VN. The Young's moduli determined using the effective elastic constant values in **Table 2** in combination with the Voigt-Reuss-Hill average are $E_{VN} = 394\pm51$ GPa and $E_{VN0.8} = 342\pm55$ GPa. The nanoindentation elastic moduli of VN and VN$_{0.8}$ – evaluated according to expression (2) in Ref. [21], together with VN$_x$ Poisson's ratios calculated using the AIMD elastic properties in **Table 2** – are $E_{VN} = 333\pm8$ GPa and $E_{VN0.8} = 316\pm11$ GPa. The relatively smaller Young's moduli of VN$_{0.8}$ is also reflected in the lower steepness of the initial slope of load/displacement curves in **Fig. 2**. We note that a higher hardness in combination to a lower Young's moduli, which is the case of VN$_{0.8}$ vs. VN, has been proposed as empirical indicator for improved toughness in ceramic coatings.

The results of AIMD simulations allow us understanding the excellent resistance to fracture of VN$_{0.8}$ in comparison to the brittleness of VN (**Fig. 3**). The propagation of atomic-scale cracks in, and fracture toughness of, solid crystals depends in a non-trivial manner on the loading condition, crack and lattice geometries, and distribution of stresses within the material [65, 66]. Generally speaking, however, crack propagation can be prevented (crack blunting) if the stress concentrated around the crack tip is rapidly dissipated by plastic flow [67]. Crack blunting may occur if the emission of dislocations at an angle to the fracture plane is sufficiently fast, that is, in relation to the speed of crack growth (bond-snapping rate) [67]. According to Schmid's law [68, 69], cracks formed on $\{001\}$ or $\{110\}$ surfaces of a B1 crystal can be blunted via $\{110\}\langle 1\bar{1}0\rangle$ and $\{111\}\langle 1\bar{1}0\rangle$ slip inclined to the fracture plane. It is reasonable to assume that the rates of dislocation

motion and crack growth are inversely related to the ideal shear and tensile strengths, respectively. Hence, the VN and $VN_{0.8}$ ability to withstand brittle cleavage on {001} and {110} planes can be assessed using the tensile-to-shear strength ratios m'·$\gamma_T^{\langle 001 \rangle}$/$\gamma_S^{\{110\}\langle 1\bar{1}0 \rangle}$ and m"·$\gamma_T^{\langle 110 \rangle}$/$\gamma_S^{\{111\}\langle 1\bar{1}0 \rangle}$, where m' = 0.5 and m" = 0.408 are the Schmid's factors for {110} and {111} slip planes with uniaxial loading along [001] and [110] directions, respectively. We suggest this ratio to be a realistic descriptor of crack resistance, analogously to the ratio of surface/unstable-stacking-fault formation energies used previously [70, 71].

The fact that the tensile/shear strength ratios calculated for $VN_{0.8}$ (≈0.7) are much larger than those (≈0.5) obtained for VN (see **Table 3**) is consistent with the superior fracture resistance of the understoichiometric compound (**Fig. 3**). We note, however, that our experimental results indicate that the toughness of $VN_{0.8}$ is *not* uniquely the result of plastic deformation. In fact, lattice slip in $VN_{0.8}$ occurs gradually, that is, to the extent necessary to prevent stress accumulation. This is demonstrated by absence of sudden pop-ins during experimental stress/strain measurements, **Fig. 2**, and by more moderate material pile-up subsequent to nanoindentation in comparison to VN, **Fig. 3c**. The fact that plastic flow (**Fig. 6**) and local structural transformations (**Figs. 4 and 5b**) in the understoichiometric compound become operative at elevated stress conditions is a requisite necessary for the simultaneous enhancement of hardness and toughness. The brittleness of VN is reflected by its lower tendency to activate lattice slip, as indicated by considerably larger shear strengths γ_S than in $VN_{0.8}$, and by the fact that stoichiometric phase undergoes sudden failure beyond its tensile yield points (**Fig. 5a**).

3.3. Electronic mechanisms of enhanced hardness and toughness in $VN_{0.8}$. DFT electronic-structure calculations provide fundamental insights for the electronic mechanisms which enhance hardness and toughness in $VN_{0.8}$. Energy-resolved electron densities, a technique for visualizing electronic states (see, e.g., Refs. [26, 72]), is here employed to demonstrate the enhancement of d-d metallic interactions in the vicinity of anion vacancies. **Fig. 7** illustrates the $VN_{0.8}$ electron densities resolved in energy intervals that primarily correspond to d-t_{2g} (**Fig. 7a**) or d-e_g states (**Fig.**

7b) near the Fermi level E_F. The energy ranges are identified by analyzing electronic densities of states (not shown). The figure demonstrates that constructive d-d wave interference (σ and π bonding states of t_{2g} and e_g symmetry, see bottom of **Fig. 7**) is favored by the presence of N vacancies (N_{vac}) both via 2nd neighbor and 4th neighbor (across N_{vac}) V–V orbital interactions. The observation that anion vacancies improve the metallic binding character in VN_x has been previously suggested for lattices with isotropic vacancy ordering [73]. Due to high metallic nature, the electron density of $VN_{0.8}$ rearranges considerably when the material is subjected to external loads comparable to its ideal tensile γ_T or shear γ_S strengths. As detailed below, strain-mediated electron transfer both leads to modifications in bonding geometries during elongation and assists lattice slip upon shearing, thus enabling rapid stress dissipation.

      Fig. 8 illustrates the electron-transfer maps calculated for $VN_{0.8}$ under tensile deformation. In **Fig. 8a**, five adjacent atomic layers are labeled in alphabetic order from "a" to "e". V and N atomic sites along each plane are numbered sequentially from "1" to "4". Note that positions "2d" and "4d" are vacant. In unstrained $VN_{0.8}(001)$, the metallic pairs V_{2c}–V_{2e} and V_{4c}–V_{4e} are linked by σ d-e_g states across vacancy sites, as schematically represented on the bottom of **Fig. 7b**. For a uniaxial strain of 20%, the electrons that formerly occupied σ d-e_g metallic states, transfer into nearest-neighbor V_{2c}–N_{2b} and V_{4c}–N_{4b} bonds parallel to the elongation, as well as 2nd-neighbor V–V σ d-t_{2g} bonds orthogonal to the deformation direction. Overall, the substantial d-electron transfer promoted by the presence of vacancies in layer "d" produces (*i*) alternating weakened/reinforced V–N bonds at "a–b" and "b–c" layer interfaces and (*ii*) stronger metallic σ d-t_{2g} binding within "a" and "c" V layers, which is evidenced by zig-zag patterned electron accumulation between all V–V pairs (**Fig. 8a**, 20% strain). **Fig. 8b** presents the $VN_{0.8}$ electronic-structure projected onto a {100} plane parallel to the elongation. The figure shows that the breakage of part of the bonds along the strain direction (note appearance of yellow-color regions in 20%-elongated $VN_{0.8}(001)$, **Fig. 8b**) results in increased electron accumulation in the remaining (reinforced) vertical V–V and V–N bonds (note, e.g., V_i–V_{ii}–N_i–V_{iii}–N_{ii} chain of bonded atoms in strained $VN_{0.8}$). The strain-

mediated electronic mechanism leads to bond-bending and buckling of (001) layers, which confer on $VN_{0.8}$ a great fracture resistance.

Our stress/strain results indicate that the initially relatively higher resistance to shearing of $VN_{0.8}$, **Fig. 6**, originates from an overall stiffening of nearest-neighbor V–N bonds. The effect is due to a larger fraction of electrons that can be employed in d-e_g–p bonding states, analogous to the vacancy-induced strengthening demonstrated for B1 $VMoN_x$ alloys (see figure 7a in [7]). However, for $\delta_{xz} > 0.09$, the $VN_{0.8}$ response to shearing changes from hard to compliant, which facilitates lattice slip. A representative example is illustrated in **Fig. 9**, where electron transfer maps are calculated for a sequence of $VN_{0.8}$ atomic configurations sampled during $\{110\}\langle 1\bar{1}0\rangle$ slip. Time progression increases in alphabetic order from **Fig. 9a** to **Fig. 9i**. The (110) atomic layer labelled as "D" slides against the (110) layer "C". Lattice slip is assisted by continuous reorganization of d-electron clouds near to N_{vac}: back and forth transfer of electrons among σ d-e_g V_2–V_3 fourth-neighbor bonds normal to the slip plane and σ d-t_{2g} V_1–V_3 second-neighbor bonds parallel to the glide direction. In particular, a shortening of the σ d-e_g V_2–V_3 bond lifts the V_3 atom upward (**Fig. 9c-g**), thus favoring lateral $[\bar{1}10]$ translation of layer "D". Presumably, N diffusion also facilitates the crystal glide process, as suggested by the fact that, while the N_1 and N_3 atoms (see **Fig. 9a-d**) migrate out of the plane of view, two additional vacancies become visible upon completion of the slip process (compare **Fig. 9a** with **Fig. 9i**).

Electronic mechanisms (not shown), similar to those described in **Fig. 9**, are likely to facilitate $\{111\}\langle 1\bar{1}0\rangle$ slip in $VN_{0.8}$ (**Fig. 6b**). However, it may be expected that, during $\{111\}\langle 1\bar{1}0\rangle$ slip, B1 $VN_{0.8}$ domains locally characterized by N contents close to 0.5 are energetically inclined to form 111 stacking faults – with -A-B-C-B- sequence – as in hexagonal $VN_{0.5}(0001)$ (space group $P\bar{3}1m$). This would provide additional degrees of freedom for $VN_{0.8}$ to dissipate mechanical stresses (analogous to the mechanism reported for metastable B1 $Ti_{0.5}W_{0.5}N(111)$ solid solutions subjected to $[1\bar{1}0]$ shearing [74]) as well as further enhance hardness by obstructing dislocation glide across the faults [75]. Last, it is worth noting that VN_x (0.74<x<0.84) compounds present

stable vacancy–ordered polymorphs [76]. Although lattice vacancies are randomly arranged in our films [19], $VN_{0.8}$ may locally activate disorder $\rightarrow$ order structural transitions in response to external loading, leading to an alternative form of transformation toughening.

4. Summary and perspectives

We combine experiments and first-principles simulations to demonstrate that the control of anion vacancy concentrations in epitaxial single-crystal B1 $VN_x(001)/MgO(001)$ ceramics allows simultaneous enhancement of both material's hardness and toughness.

Berkovich nanoindentation, used to measure the films' hardness, shows that understoichiometric $VN_{0.8}$ is $\approx20\%$ harder than stoichiometric VN samples. The materials' fracture toughness is qualitatively assessed by cube-corner nanoindentation, performed at constant penetrations which largely exceed the films' thickness. These tests demonstrate that, while VN fractures in a brittle manner, the understoichiometric $VN_{0.8}$ compound *never* cracks.

First-principles atomistic modeling of supercells subjected to tensile and shear deformation allows us rationalizing the dramatic differences in the mechanical behavior of VN vs. $VN_{0.8}$. Our results show that $VN_{0.8}$ possesses higher elastic shear stiffness than VN, which may explain its greater measured hardness. However, despite its initially higher resistance to change of shape, $VN_{0.8}$ requires considerably lower shear stresses than VN to induce $\{110\}\langle1\bar{1}0\rangle$ and $\{111\}\langle1\bar{1}0\rangle$ lattice slip at room temperature. For supercells subjected to uniaxial elongation, AIMD simulations show that, while stoichiometric VN crystals suddenly cleave at their yield point, the understoichiometric compound activates local lattice transformations, which reflect its superior toughness.

Thorough analyses of the $VN_{0.8}$ electronic structures indicate that (*i*) the high elastic resistance to shearing originates from intrinsically stronger first-neighbor V–N bonds, whereas (*ii*) the ability to dissipate accumulated external stresses by inducing structural transformations and lattice slip stems from the possibility of mutually transferring electrons among 2nd- and 4th-neighbor

(across vacancy) V–V metallic states. In contrast, the relative softness of the stoichiometric compound originates from electronic/phonon instabilities which facilitate B1→tetragonal martensitic phase transitions upon shearing in the elastic-response regime.

It would be reasonable to assume that a vacancy-induced enhancement in metallic character of anion-deficient B1 TM carbonitrides – evidenced by the increased x-ray photoelectron spectra intensities at low binding energies [9, 77-81] – necessarily implies improved plasticity. However, rigorous experimental testing should be performed to verify whether the material's toughness is effectively increased by an enhanced metallic-bonding character, i.e., exclude a concomitant drop in hardness. In this regard, although experimental results consistently show that anion vacancies harden B1 Group-VB carbonitrides, conflicting trends in H vs. vacancy concentration have been reported for Group-IVB carbonitrides [16, 28, 82-84]. Rationale design of hard and tough carbonitrides should aim at triggering the material's plastic response at the *right stage* of a deformation process: *too early* would imply softness; *too late* may cause brittle fracture. We foresee that the concentration of valence electrons is a key parameter to control the hard → plastic turning point under loading. This study offers a novel strategy to identify alloy and/or multicomponent (high-entropy) refractory carbides and nitrides with superior combination of hardness and toughness.

References

[1] W.J. Clegg, Controlling cracks in ceramics, Science 286 (1999) 1097.

[2] A. Kelly, W.R. Tyson, A.H. Cottrell, Ductile and brittle crystals, Philosophical Magazine 15 (1967) 567.

[3] W.D. Callister, D.G. Rethwisch, Materials science and engineering, John Wiley & Sons NY (2011).

[4] A.A. Voevodin, J.S. Zabinski, Supertough wear-resistant coatings with 'chameleon' surface adaptation, Thin Solid Films 370 (2000) 223.

[5] T.S. Oh, J. Rodel, R.M. Cannon, R.O. Ritchie, Ceramic metal interfacial crack-growth - toughening by controlled microcracks and interfacial geometries, Acta Metallurgica 36 (1988) 2083.

[6] H. Kindlund, D.G. Sangiovanni, L. Martinez-de-Olcoz, J. Lu, J. Jensen, J. Birch, I. Petrov, J.E. Greene, V. Chirita, L. Hultman, Toughness enhancement in hard ceramic thin films by alloy design, APL Materials 1 (2013) 042104.

[7] H. Kindlund, D.G. Sangiovanni, J. Lu, J. Jensen, V. Chirita, J. Birch, I. Petrov, J.E. Greene, L. Hultman, Vacancy-induced toughening in hard single-crystal $V_{0.5}Mo_{0.5}N_x$/MgO(001) thin films, Acta Materialia 77 (2014) 394.

[8] H. Kindlund, J. Lu, E. Broitman, I. Petrov, J.E. Greene, J. Birch, L. Hultman, Growth and mechanical properties of 111-oriented $V_{0.5}Mo_{0.5}N_x$/Al$_2$O$_3$(0001) thin films, Journal of Vacuum Science & Technology A 36 (2018) 051512.

[9] H. Kindlund, G. Greczynski, E. Broitman, L. Martínez-de-Olcoz, J. Lu, J. Jensen, I. Petrov, J.E. Greene, J. Birch, L. Hultman, $V_{0.5}Mo_{0.5}N_x$/MgO(001): Composition, nanostructure, and mechanical properties as a function of film growth temperature, Acta Materialia 126 (2017) 194.

[10] M.A. Meyers, K.K. Chawla, Mechanical Behavior of Materials, Prentice Hall, Englewood Cliffs (1999).

[11] G.E. Dieter, Mechanical Metallurgy, second ed., McGraw-Hill (1976).

[12] H.Y. Niu, X.Q. Chen, P.T. Liu, W.W. Xing, X.Y. Cheng, D.Z. Li, Y.Y. Li, Extra-electron induced covalent strengthening and generalization of intrinsic ductile-to-brittle criterion, Scientific Reports 2 (2012) 718.

[13] R.O. Ritchie, The conflicts between strength and toughness, Nature Materials 10 (2011) 817.

[14] G. Farges, E. Beauprez, M.C. Stecatherine, Crystallographic structure of sputtered cubic δ-VN_x films - influence of basic deposition parameters, Surface & Coatings Technology 61 (1993) 238.

[15] M. Benkahoul, E. Martinez, A. Karimi, R. Sanjines, F. Levy, Structural and mechanical properties of sputtered cubic and hexagonal NbN_x thin films, Surface & Coatings Technology 180 (2004) 178.

[16] H. Holleck, Material selection for hard coatings, Journal of Vacuum Science & Technology A 4 (1986) 2661.

[17] R. Sanjines, C. Wiemer, P. Hones, F. Levy, Chemical bonding and electronic structure in binary VN_y and ternary $T_{1-x}V_xN_y$ nitrides, Journal of Applied Physics 83 (1998) 1396.

[18] A.B. Mei, R.B. Wilson, D. Li, D.G. Cahill, A. Rockett, J. Birch, L. Hultman, J.E. Greene, I. Petrov, Elastic constants, Poisson ratios, and the elastic anisotropy of VN(001), (011), and (111) epitaxial layers grown by reactive magnetron sputter deposition, Journal of Applied Physics 115 (2014) 214908.

[19] A.B. Mei, M. Tuteja, D.G. Sangiovanni, R.T. Haasch, A. Rockett, L. Hultman, I. Petrov, J.E. Greene, Growth, nanostructure, and optical properties of epitaxial VN_x/MgO(001) ($0.80 \leq x \leq 1.00$) layers deposited by reactive magnetron sputtering, Journal of Materials Chemistry C 4 (2016) 7924.

[20] Q. Zheng, A.B. Mei, M. Tuteja, D.G. Sangiovanni, L. Hultman, I. Petrov, J.E. Greene, D.G. Cahill, Phonon and electron contributions to the thermal conductivity of VN_x epitaxial layers, Physical Review Materials 1 (2017) 065002.

[21] W.C. Oliver, G.M. Pharr, An improved technique for determining hardness and elastic-modulus using load and displacement sensing indentation experiments, Journal of Materials Research 7 (1992) 1564.

[22] E. Broitman, Indentation hardness measurements at macro-, micro-, and nanoscale: a critical overview, Tribology Letters 65 (2017) 23.

[23] Y. Gogotsi, V. Domnich, High Pressure Surface Science and Engineering, CRC Press (2003).

[24] R. Car, M. Parrinello, Unified approach for molecular dynamics and density-functional theory, Physical Review Letters 55 (1985) 2471.

[25] W. Liu, X. Liu, W.T. Zheng, Q. Jiang, Surface energies of several ceramics with NaCl structure, Surface Science 600 (2006) 257.

[26] S.H. Jhi, J. Ihm, S.G. Louie, M.L. Cohen, Electronic mechanism of hardness enhancement in transition-metal carbonitrides, Nature 399 (1999) 132.

[27] S.H. Jhi, S.G. Louie, M.L. Cohen, J.W. Morris, Mechanical instability and ideal shear strength of transition metal carbides and nitrides, Physical Review Letters 87 (2001) 075503.

[28] S.H. Jhi, S.G. Louie, M.L. Cohen, J. Ihm, Vacancy hardening and softening in transition metal carbides and nitrides, Physical Review Letters 86 (2001) 3348.

[29] R.H.J. Hannink, D.L. Kohlstedt, M.J. Murray, Slip system determination in cubic carbides by hardness anisotropy, Proc. R. Soc. Lond. A 326 (1972) 409.

[30] L.E. Toth, Transition Metal Carbides and Nitrides, Academic Press, New York (1971).

[31] L. Hultman, M. Shinn, P.B. Mirkarimi, S.A. Barnett, Characterization of misfit dislocations in epitaxial (001)-oriented TiN, NbN, VN, and (Ti,Nb)N film heterostructures by transmission electron-microscopy, Journal of Crystal Growth 135 (1994) 309.

[32] G. Kresse, J. Furthmuller, Efficient iterative schemes for *ab initio* total-energy calculations using a plane-wave basis set, Physical Review B 54 (1996) 11169.

[33] P.E. Blöchl, Projector augmented-wave method, Physical Review B 50 (1994) 17953.

[34] J.P. Perdew, K. Burke, M. Ernzerhof, Generalized gradient approximation made simple, Physical Review Letters 77 (1996) 3865.

[35] M. Parrinello, A. Rahman, Polymorphic transitions in single-crystals - a new molecular dynamics method, Journal of Applied Physics 52 (1981) 7182.

[36] D.G. Sangiovanni, Inherent toughness and fracture mechanisms of refractory transition-metal nitrides via density-functional molecular dynamics, Acta Materialia 151 (2018) 11.

[37] D.G. Sangiovanni, F. Tasnadi, L.J.S. Johnson, M. Oden, I.A. Abrikosov, Strength, transformation toughening and fracture dynamics of rocksalt-structure $Ti_{1-x}Al_xN$ ($0 \leq x \leq 0.75$) alloys, Physical Review Materials (2020) *accepted*.

[38] D. Roundy, C.R. Krenn, M.L. Cohen, J.W. Morris, Ideal shear strengths of fcc aluminum and copper, Physical Review Letters 82 (1999) 2713.

[39] A.B. Mei, O. Hellman, N. Wireklint, C.M. Schlepütz, D.G. Sangiovanni, B. Alling, A. Rockett, L. Hultman, I. Petrov, J.E. Greene, Dynamic and structural stability of cubic vanadium nitride, Physical Review B 91 (2015) 054101.

[40] W. Humphrey, A. Dalke, K. Schulten, VMD: Visual molecular dynamics, Journal of Molecular Graphics & Modelling 14 (1996) 33.

[41] J.R. Morris, H. Bei, G.M. Pharr, E.P. George, Size effects and stochastic behavior of nanoindentation pop in, Physical Review Letters 106 (2011) 165502.

[42] C.A. Schuh, A.C. Lund, Application of nucleation theory to the rate dependence of incipient plasticity during nanoindentation, Journal of Materials Research 19 (2004) 2152.

[43] C. Berejnoi, J.E.P. Ipina, An alternative method for small pop-in assessment, Engineering Fracture Mechanics 59 (1998) 667.

[44] B.R. Lawn, N.P. Padture, F. Guiberteau, H. Cai, A model for micropack initiation and propagation beneath hertzian contacts in polycrystalline ceramics, Acta Metallurgica Et Materialia 42 (1994) 1683.

[45] D.J. Oliver, B.R. Lawn, R.F. Cook, M.G. Reitsma, J.E. Bradby, J.S. Williams, P. Munroe, Giant pop-ins in nanoindented silicon and germanium caused by lateral cracking, Journal of Materials Research 23 (2008) 297.

[46] W.W. Gerberich, J.C. Nelson, E.T. Lilleodden, P. Anderson, J.T. Wyrobek, Indentation induced dislocation nucleation: The initial yield point, Acta Materialia 44 (1996) 3585.

[47] B. Eidel, Crystal plasticity finite-element analysis versus experimental results of pyramidal indentation into (001) fcc single crystal, Acta Materialia 59 (2011) 1761.

[48] U_T is the energy density absorbed during deformation: area that underlies a stress/strain curve in **Fig. 4**.

[49] It has been shown that the dislocation-core structures exhibit complex polymorph variants and depend on local stoichiometries in ceramic oxides [50-52]. Atomic-level knowledge of these structures is currently lacking for refractory nitrides. Nonetheless, the application of uniform shear deformation to dislocation-free VN and $VN_{0.8}$ lattices allows us probing the effects induced by anion vacancies on the compound elastic shear stiffness, ideal shear strengths γ_s, and intrinsic ability to activate lattice slip.

[50] Z.C. Wang, M. Saito, K.P. McKenna, Y. Ikuhara, Polymorphism of dislocation core structures at the atomic scale, Nature Communications 5 (2014) 3239.

[51] E. Maras, M. Saito, K. Inoue, H. Jonsson, Y. Ikuhara, K.P. McKenna, Determination of the structure and properties of an edge dislocation in rutile TiO_2, Acta Materialia 163 (2019) 199.

[52] Y. Furushima, Y. Arakawa, A. Nakamura, E. Tochigi, K. Matsunaga, Nonstoichiometric 012 dislocation in strontium titanate, Acta Materialia 135 (2017) 103.

[53] P.C. Dokko, J.A. Pask, Plastic-deformation of ceramic materials, Materials Science and Engineering 25 (1976) 77

[54] Q.-M. Hu, K. Kadas, S. Hogmark, R. Yang, B. Johansson, L. Vitos, Hardness and elastic properties of covalent/ionic solid solutions from first-principles theory, Journal of Applied Physics 103 (2008) 083505.

[55] Y. Tian, B. Xu, Z. Zhao, Microscopic theory of hardness and design of novel superhard crystals, International Journal of Refractory Metals & Hard Materials 33 (2012) 93.

[56] D. Holec, M. Friak, J. Neugebauer, P.H. Mayrhofer, Trends in the elastic response of binary early transition metal nitrides, Physical Review B 85 (2012) 064101.

[57] The correspondence between stresses $\bar{S}$ recorded during AIMD mechanical testing and the cubic elastic constants $\bar{C}$ is described by $\bar{\bar{A}} \cdot \bar{C} = \bar{S}$, where: $\bar{\bar{A}}$ = {(0, 1, 0), (0, 1, 0), (1, 0, 0), (1/2, 1/2, –1), (0, 1, 0), (1/2, 1/2, 1), (1/2, –1/2, 0), (–√2/6, √2/6, √2/3), (1/3, –1/3, 1/3)}; $\bar{C}$= (C_{11}, C_{12}, C_{44}); $\bar{S}$ = ($\sigma_{xx}^{\langle 001 \rangle}$, $\sigma_{yy}^{\langle 001 \rangle}$, $\sigma_{zz}^{\langle 001 \rangle}$, $\sigma_{xx}^{\langle 110 \rangle}$, $\sigma_{yy}^{\langle 110 \rangle}$, $\sigma_{zz}^{\langle 110 \rangle}$, $\sigma_{xz}^{\{110\}\langle 1\bar{1}0 \rangle}$, $\sigma_{xy}^{\{111\}\langle 1\bar{1}0 \rangle}$, $\sigma_{xz}^{\{111\}\langle 1\bar{1}0 \rangle}$). AIMD *effective* (or average) elastic constants $\widetilde{C}_{ij}$ are obtained by norm minimization, i.e., $\widetilde{C}_{ij}$ = minc$\|\bar{\bar{A}} \cdot \bar{C} - \bar{S}\|$. The *actual* elastic stiffnesses are, instead, explicitly calculated from the initial (≤2% deformation) slopes of stress vs. strain curves: σ_{zz} during [001] elongation → C_{11}, σ_{xz} during $\{110\}\langle 1\bar{1}0 \rangle$ shearing → G_{110}, and σ_{xz} during $\{111\}\langle 1\bar{1}0 \rangle$ shearing → G_{111u}.

[58] The subscript "u" in G_{111u} indicates that this is an unrelaxed shear moduli, i.e., calculated by imposing $\{111\}\langle 1\bar{1}0 \rangle$ shear deformation without relaxing stress components other than σ_{xz}. In simulations that alllow relaxation, the correspondent shear moduli would be G_{111r} = $3 \cdot C_{44} \cdot (C_{11} - C_{12})/(C_{11} - C_{12} + 4 \cdot C_{44})$.

[59] The relationships that link the C_{11}, C_{12}, C_{44}, G_{110}, G_{111u} elastic constants and moduli to the stress components σ_{ij} recorded during AIMD mechanical testing that applies a generic

deformation (δ_{ij}) to a supercell with generic orientation, are determined by appropriate rotations (R) of σ and δ matrixes. The stress (σ') and strain (δ') tensors in a coordinate system with $\langle 001 \rangle$ crystallographic axes parallel to x, y, and z Cartesian directions are calculated via: $\sigma' = R \cdot \sigma \cdot R_{-1}$ and $\delta' = R \cdot \delta \cdot R_{-1}$. Note that two different rotations need to be applied in the case of deformation applied to supercells with [111] vertical orientation.

[60] We note that the choice of the vacancy arrangements in $VN_{0.8}$ supercells may affect the results of elastic constants, as described in Ref. [61].

[61] D. Edström, D.G. Sangiovanni, L. Hultman, V. Chirita, Effects of atomic ordering on the elastic properties of TiN- and VN-based ternary alloys, Thin Solid Films 571 (2014) 145.

[62] D.G. Sangiovanni, Mass transport properties of quasiharmonic vs. anharmonic transition-metal nitrides, Thin Solid Films 688 (2019) 137297.

[63] F. Kubel, W. Lengauer, K. Yvon, K. Knorr, A. Junod, Structural phase-transition at 205 K in stoichiometric vanadium nitride, Physical Review B 38 (1988) 12908.

[64] P. Rehak, M. Cerny, D. Holec, Interface-induced electronic structure toughening of nitride superlattices, Surface & Coatings Technology 325 (2017) 410.

[65] M.J. Alava, P. Nukalaz, S. Zapperi, Statistical models of fracture, Advances in Physics 55 (2006) 349.

[66] T. Nguyen, D. Bonamy, Role of the crystal lattice structure in predicting fracture toughness, Physical Review Letters 123 (2019) 205503.

[67] J.R. Rice, R. Thomson, Ductile versus brittle behaviour of crystals, Philosophical Magazine 29 (1974) 73.

[68] Schmid's factors (m) resolve the applied shear stress onto different crystallographic directions.

[69] For B1 crystals, the Burgers vector is the shortest lattice spacing along $\langle 110 \rangle$ directions. Schmid's factors on $\{110\}$ slip planes for loading along $\langle 001 \rangle$ and $\langle 110 \rangle$ directions are 0.5 and 0.25, respectively [see table 2 in S. Kiani, J.-M. Yang, S. Kodambaka, Nanomechanics of Refractory Transition-Metal Carbides: A Path to Discovering Plasticity in Hard Ceramics, Journal of the American Ceramic Society 98 (2015) 2313]. For slip of $\{111\}$ planes, instead, the Schmid's factors are 0.408 in both cases.

[70] U.V. Waghmare, E. Kaxiras, V.V. Bulatov, M.S. Duesbery, Effects of alloying on the ductility of $MoSi_2$ single crystals from first-principles calculations, Modelling and Simulation in Materials Science and Engineering 6 (1998) 493.

[71] J.R. Rice, G.E. Beltz, The activation-energy for dislocation nucleation at a crack, Journal of the Mechanics and Physics of Solids 42 (1994) 333.

[72] M. Mikula, M. Truchlý, D.G. Sangiovanni, D. Plašienka, T. Roch, M. Gregor, P. Ďurina, M. Janík, P. Kúš, Experimental and computational studies on toughness enhancement in Ti-Al-Ta-N quaternaries, Journal of Vacuum Science & Technology A 35 (2017) 060602.

[73] L. Benco, Chemical bonding in stoichiometric and substoichiometric vanadium nitride, Journal of Solid State Chemistry 110 (1994) 58.

[74] D.G. Sangiovanni, L. Hultman, V. Chirita, I. Petrov, J.E. Greene, Effects of phase stability, lattice ordering, and electron density on plastic deformation in cubic TiWN pseudobinary transition-metal nitride alloys, Acta Materialia 103 (2016) 823.

[75] H.W. Hugosson, U. Jansson, B. Johansson, O. Eriksson, Restricting dislocation movement in transition metal carbides by phase stability tuning, Science 293 (2001) 2434.

[76] T. Onozuka, Vacancy ordering in VN_{1-x}, Journal of Applied Crystallography 11 (1978) 132.

[77] L. Porte, L. Roux, J. Hanus, Vacancy effects in the x-ray photoelectron spectra of TiN_x, Physical Review B 28 (1983) 3214.

[78] L. Porte, Electronic structure of non-stoichiometric zirconium nitrides ZrN_x, Solid state communications 50 (1984) 303.

[79] J. Redinger, P. Marksteiner, P. Weinberger, Vacancy-induced changes in the electronic structure of transition metal carbides and nitrides: calculation of x-ray photoemission intensities, Zeitschrift für Physik B Condensed Matter 63 (1986) 321.

[80] G. Greczynski, H. Kindlund, I. Petrov, J. Greene, L. Hultman, Sputter-cleaned epitaxial $V_xMo_{1-x}N_y$/MgO(001) thin films analyzed by x-ray photoelectron spectroscopy: 1. Single-crystal $V_{0.48}Mo_{0.52}N_{0.64}$, Surface Science Spectra 20 (2013) 68.

[81] G. Greczynski, H. Kindlund, I. Petrov, J. Greene, L. Hultman, Sputter-cleaned epitaxial $V_xMo_{1-x}N_y$/MgO(001) thin films analyzed by x-ray photoelectron spectroscopy: 2. Single-crystal $V_{0.47}Mo_{0.53}N_{0.92}$, Surface Science Spectra 20 (2013) 74.

[82] C.S. Shin, D. Gall, N. Hellgren, J. Patscheider, I. Petrov, J.E. Greene, Vacancy hardening in single-crystal TiN_x(001) layers, Journal of Applied Physics 93 (2003) 6025.

[83] K.C. Han, G.Q. Lin, C. Dong, Y.Q. Liu, Nitrogen concentration dependent mechanical properties of TiN_x single-phase films ($0.75 \leq x \leq 0.99$), Ceramics International 42 (2016) 10332.

[84] C.Q. Hu, X.B. Zhang, Z.Q. Gu, H.H. Huang, S. Zhang, X.F. Fan, W. Zhang, Q. Wei, W.T. Zheng, Negative effect of vacancies on cubic symmetry, hardness and conductivity in hafnium nitride films, Scripta Materialia 108 (2015) 141.

[85] J.O. Kim, J.D. Achenbach, P.B. Mirkarimi, M. Shinn, S.A. Barnett, Elastic-constants of single-crystal transition-metal nitride films measured by line-focus acoustic microscopy, Journal of Applied Physics 72 (1992) 1805.

[86] Y.-C. Lee, J.O. Kim, J.D. Achenbach, Acoustic microscopy measurement of elastic constants and mass density, Ultrasonics, Ferroelectrics and Frequency Control, IEEE Transactions 42 (1995) 253.

[87] K. Balasubramanian, S.V. Khare, D. Gall, Valence electron concentration as an indicator for mechanical properties in rocksalt structure nitrides, carbides and carbonitrides, Acta Materialia 152 (2018) 175 (see also supplemental material of the paper).

[88] W. Weber, P. Roedhammer, L. Pintschovius, W. Reichardt, F. Gompf, A.N. Christensen, Phonon anomalies in vn and their electronic origin, Physical Review Letters 43 (1979) 868.

[89] C_{11} and C_{12} values are also calculated from the slopes of $VN_{0.86}$ phonon branches shown in figure 1 of [88]. The frequency vs. q data have been extracted from the figure using the open-source software Plot Digitizer [90]. Linear regression of phonon-frequency vs. q-vector-lengths data ($\rightarrow$ acoustic velocities v_{hkl}), together with a $VN_{0.86}$ lattice parameter ($a = q_{-1} = 4.105$ Å) and mass density (ρ=6035 kg·m$_{-3}$) taken from table 1 in Ref. [20], allows us to extract $[C_{ij} = v_{hkl2} \cdot \rho]$ the C_{11}, C_{12}, and C_{44} elastic constants via the relationships listed in table 1 of [91].

[90] A.J. Kadic, K. Vucic, S. Dosenovic, D. Sapunar, L. Puljak, Extracting data from figures with software was faster, with higher interrater reliability than manual extraction, Journal of Clinical Epidemiology 74 (2016) 119.

[91] D.C. Wallace, Thermoelasticity of Stressed Materials and Comparison of Various Elastic Constants, Physical Review 162 (1967) 776.

[92] D.G. Sangiovanni, L. Hultman, V. Chirita, Supertoughening in B1 transition metal nitride alloys by increased valence electron concentration, Acta Materialia 59 (2011) 2121.

[93] Using the density of understoichiometric VN_x samples (5970 and 5980 kg·m$_{-3}$) published in [86], we estimate N compositions x $\approx$ 0.7 - 0.8.

[94] We have performed additional DFT calculations at 0 K (400 eV cutoff energy) for $\{110\}\langle 1\bar{1}0 \rangle$ and $\{111\}\langle 1\bar{1}0 \rangle$ deformation of the supercells used in AIMD. We obtained $G_{110} = 310$ GPa and $G_{111u} = 270$ GPa.

	$\gamma_{T/S}$ (GPa)	$\delta_{T/S}$ (%)	U_T (GPa)
VN			
Tensile $\langle 001 \rangle$	36	14	3.6
Tensile $\langle 110 \rangle$	46	16	4.7
Shear $\{110\}\langle 1\bar{1}0 \rangle$	34	18	
Shear $\{111\}\langle 1\bar{1}0 \rangle$	39	22	
VN$_{0.8}$			
Tensile $\langle 001 \rangle$	32	30	7.6
Tensile $\langle 110 \rangle$	42	23	6.2
Shear $\{110\}\langle 1\bar{1}0 \rangle$	23	14	
Shear $\{111\}\langle 1\bar{1}0 \rangle$	25	18	

Table 1. Ideal tensile and shear strengths γ_T and γ_S, tensile toughness U_T, and yield strains δ_T and δ_S of B1 VN$_x$ crystals determined by AIMD simulations at 300 K.

	C_{11} (GPa)	C_{12} (GPa)	C_{44} (GPa)	G_{110} (GPa)	G_{111u} (GPa)
VN					
Actual **stiffness C_{ij}, G_{hkl}**	**606±8**	-	*	**116±13**	**94±18**
Effective stiffness $\widetilde{C}_{ij}$, $\widetilde{G}_{hkl}$	603±20	258±37	135±18	172±21	193±15
Exper. & DFT	533–623	135–251	122–196	186–325	158–266
VN$_{0.8}$					
Actual **stiffness C_{ij}, G_{hkl}**	**476±15**	-	*	**205±7**	**190±7**
Effective stiffness $\widetilde{C}_{ij}$, $\widetilde{G}_{hkl}$	509±36	168±22	111±24	171±21	151±16
Exper. & DFT	512–555	113–165	127–240	195–315	164–285

Table 2. Elastic constants C_{ij} and shear moduli G_{hkl} of B1 VN and VN$_{0.8}$ determined by present AIMD simulations at room temperature [57] vs. previous experimental and 0-K DFT results [18, 85-94]. The statistical uncertainty on C_{11}, G_{110}, and G_{111u} values accounts for stress fluctuations during AIMD. *Not calculated: direct evaluation of the *actual* C_{44} [$\equiv G_{001}$] shear stiffness requires modelling $\{001\}\langle 1\bar{1}0 \rangle$ shear deformation.

	$m' \cdot \gamma_T^{\langle 001 \rangle} / \gamma_S^{\{110\}\langle 1\bar{1}0 \rangle}$	$m'' \cdot \gamma_T^{\langle 110 \rangle} / \gamma_S^{\{111\}\langle 1\bar{1}0 \rangle}$
VN	0.53	0.48
VN$_{0.8}$	0.70	0.69

Table 3. Calculated tensile-to-shear strength ratios, here used as indicators of fracture resistance.

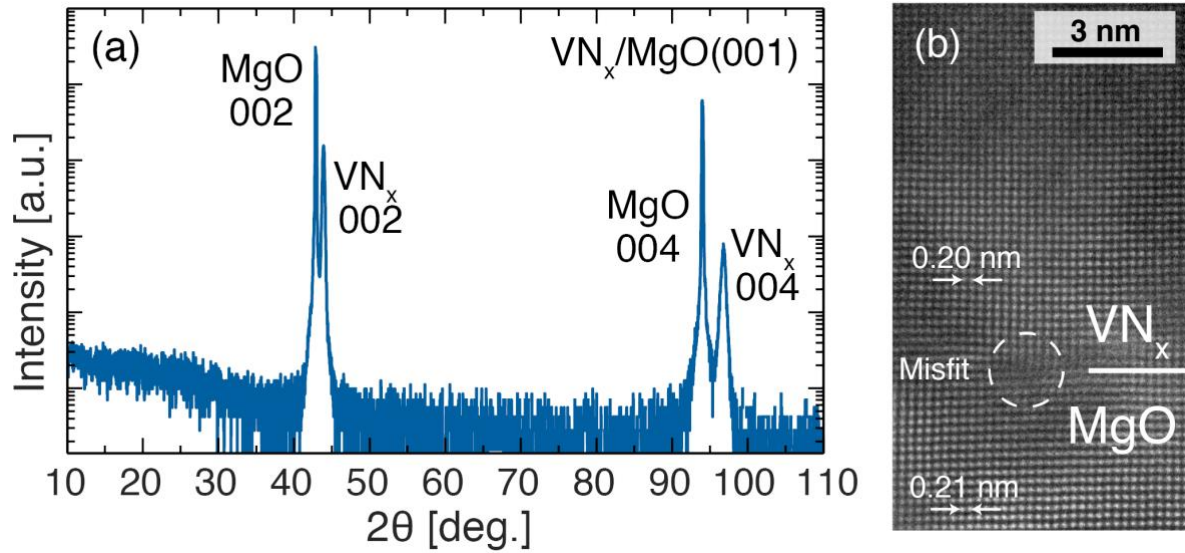**Fig. 1. (a)** XRD ω-2θ scan from a 300-nm-thick understoichiometric VN$_{0.8}$/MgO(001) layer. Four peaks are present, consistent with an epitaxial single-crystalline film. **(b)** HR-XTEM micrograph acquired near the film/substrate interface and along the [100] zone axis of a VN/MgO(001) film. A misfit dislocation is encircled in panel **(b)**.

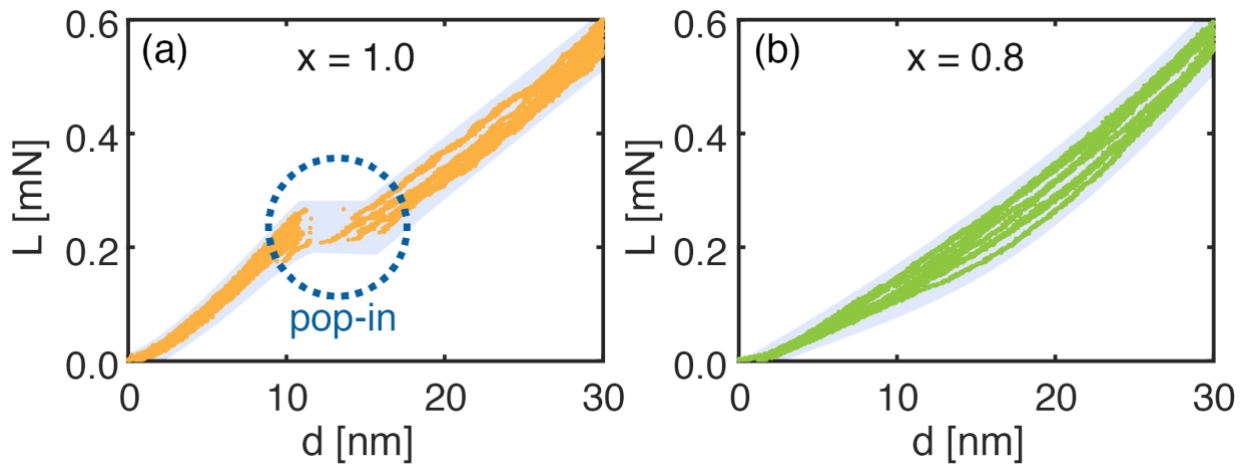**Fig. 2.** Typical load-displacement curves L(d) obtained from nanoindentations of 300-nm-thick VN$_x$/MgO(001) films with **(a)** x = 1.0 and **(b)** x = 0.8. Pop-ins signaling catastrophic material failure at the mesoscopic scale are observed only in stoichiometric films.
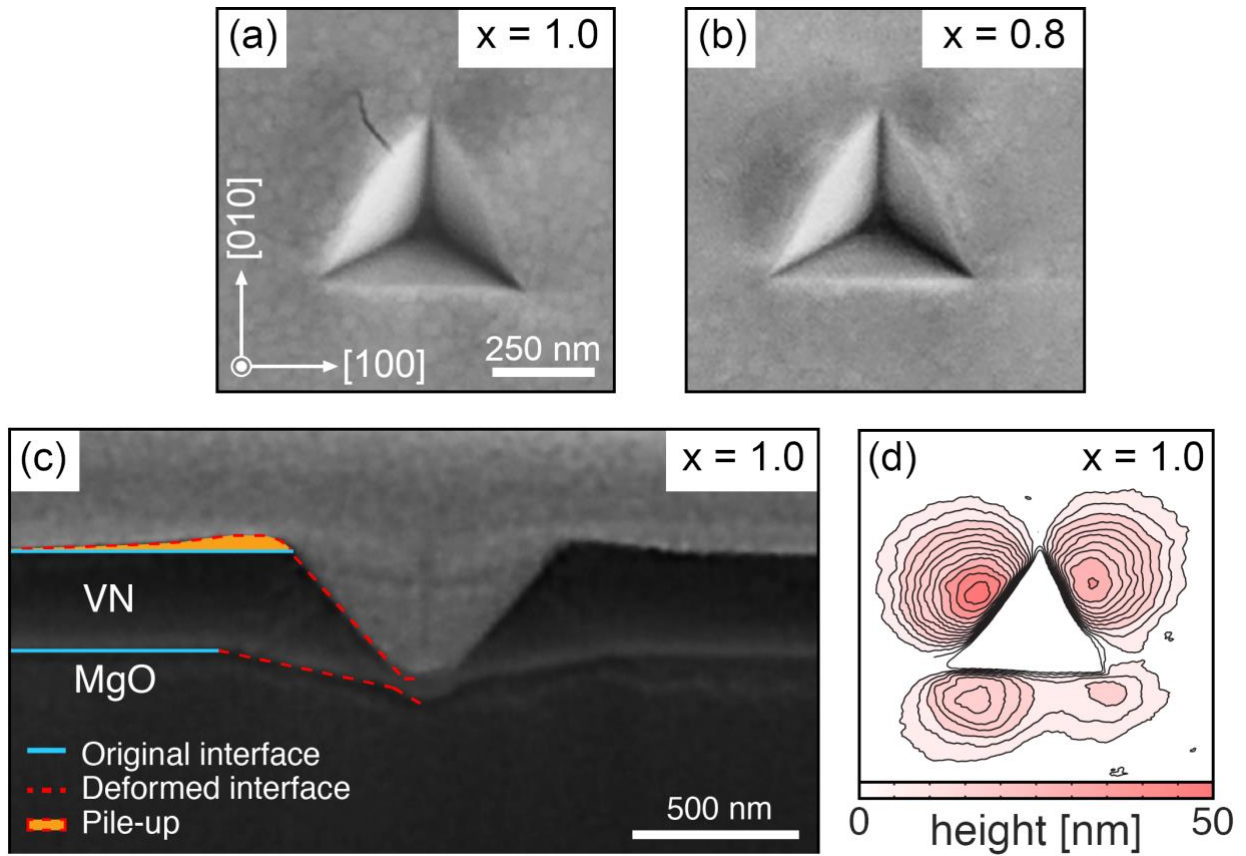
Fig. 3. SEM images of 400-nm-deep cube-corner indentations of 300-nm-thick $VN_x/MgO(001)$ layers with N contents **(a)** x = 1.0 and **(b)** x = 0.8. **(c)** Cross-sectional SEM image of the indent in panel **(a)**. The vertical section is cut using a focused Ga_+ ion beam. **(d)** SPM height isointensity contours of the indent in panel **(a)** showing material pile-up along <110> directions. The mounds retain their X-pattern while the triangular indentor probe is rotated around the indentation axis. The results shown for VN/MgO(001) in **(d)** are also representative for $VN_{0.8}/MgO(001)$.
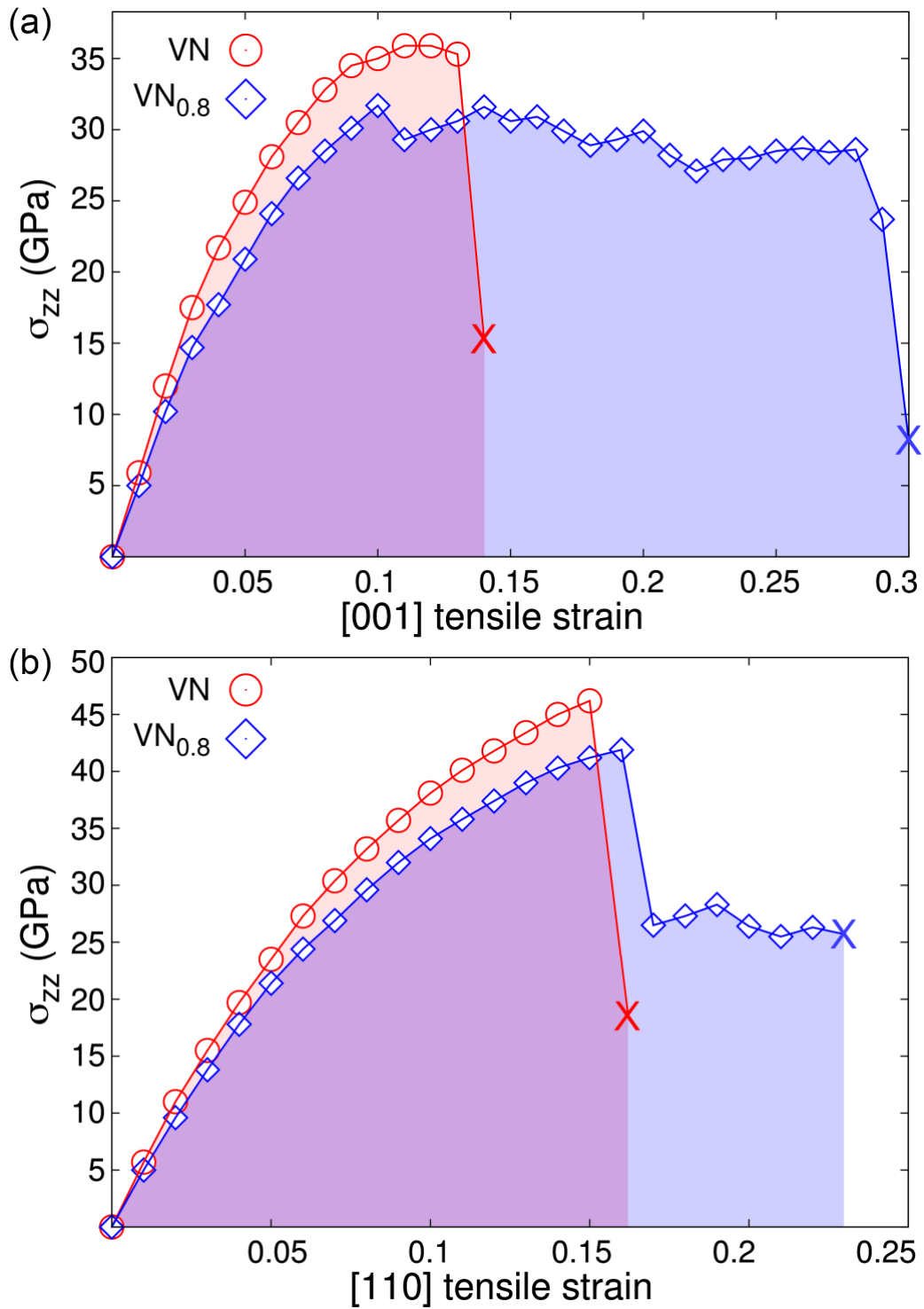
Fig. 4. Tensile stress σ_{zz} determined as a function of tensile strain along **(a)** [001] and **(b)** [110] directions by AIMD simulations at 300 K for VN and VN$_{0.8}$. Fracture points are indicated by "×" symbols. For both elongation directions, the understoichiometric compound exhibits superior toughness (indicated by colored shaded areas) than VN.
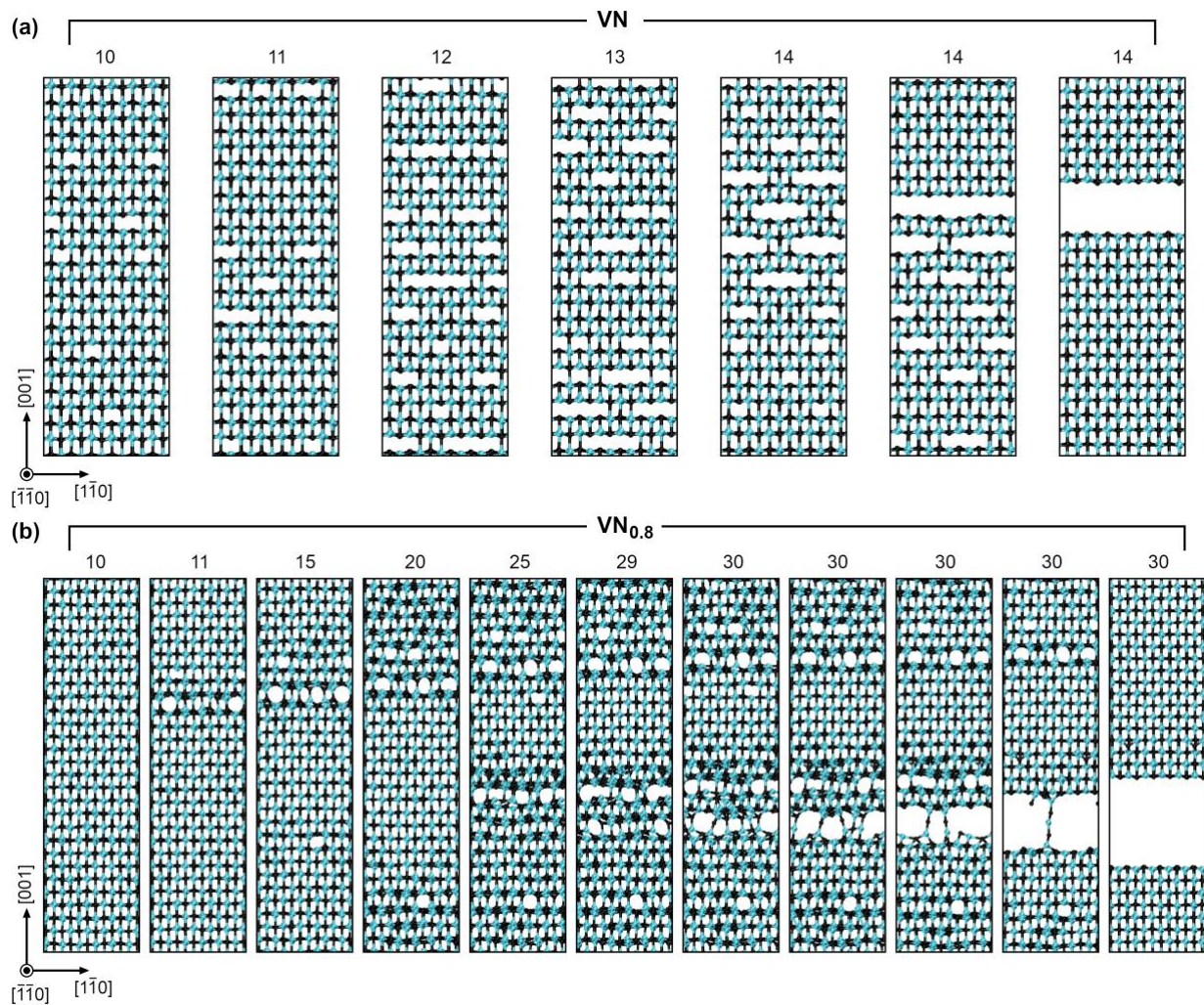
Fig. 5. AIMD snapshots during [001] tensile-loading of **(a)** stoichiometric VN(001) and **(b)** understoichiometric $VN_{0.8}$(001). Vanadium and nitrogen atoms are represented as cyan and black spheres. Each panel is labeled by numbers that indicate elongation percentages δ_{zz}. Cleavage of the crystals on (001) planes can be visualized in a sequence of snapshots at constant strains, separated by fractions of ps. While VN fractures at $\delta_T = 14\%$, understoichiometric $VN_{0.8}$ sustains elongation up to 30% without cracking. Strain-mediating structural transformations in $VN_{0.8}$ result in enhanced (dislocation-free) plasticity.
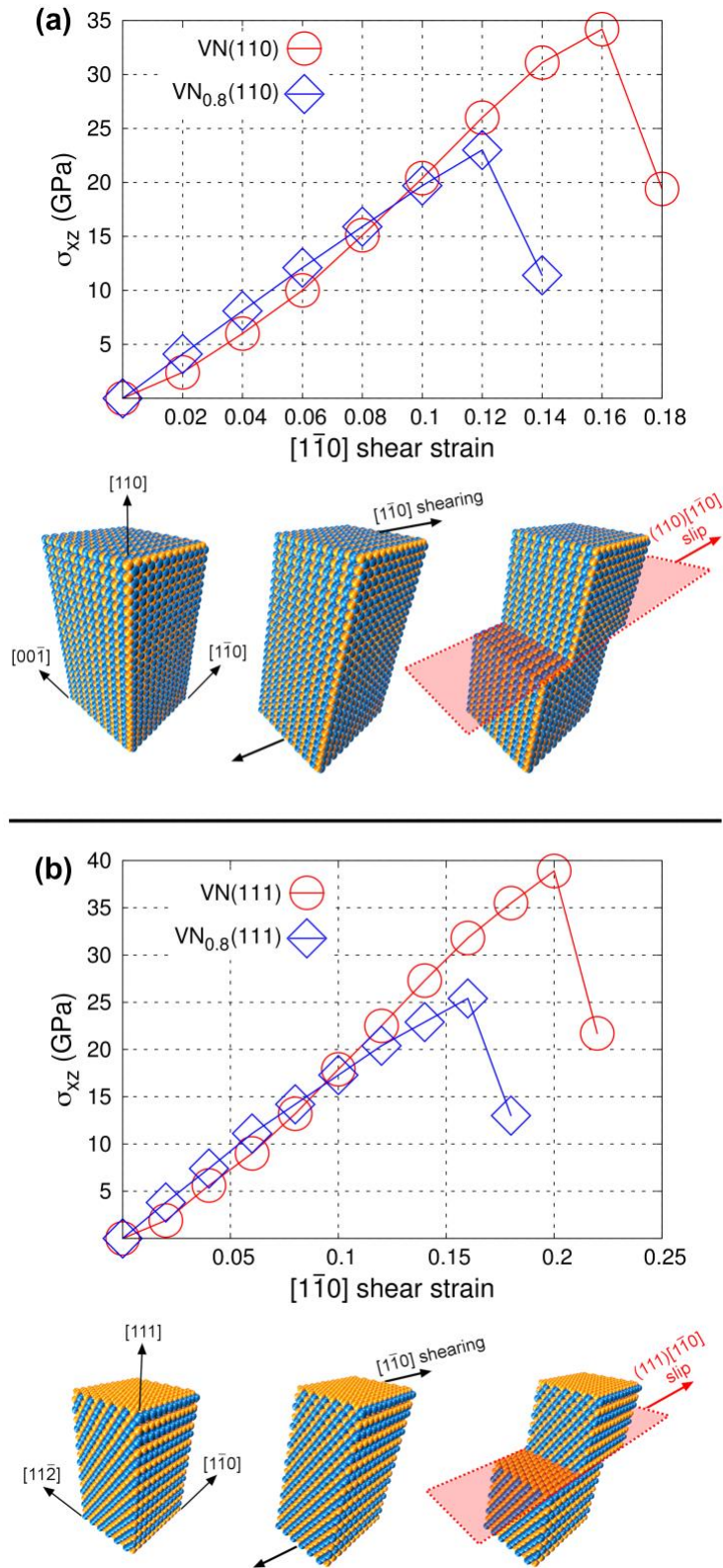
Fig. 6. AIMD stress/strain curves calculated at 300 K during shearing of **(a)** VN(110) and VN$_{0.8}$(110) and **(b)** VN(111) and VN$_{0.8}$(111) along the Burgers vector direction [1$\bar{1}$0] up to the occurrence of lattice slip (note drops in shear stress σ_{xz} at curve extremities). $\{110\}\langle 1\bar{1}0\rangle$ and $\{111\}\langle 1\bar{1}0\rangle$ shearing and lattice slip are schematically illustrated in the lower part of each panel. For both $\{110\}\langle 1\bar{1}0\rangle$ and $\{111\}\langle 1\bar{1}0\rangle$ slip systems, VN$_{0.8}$ exhibits an initially stronger resistance to shear deformation (up to ≈9%), followed by more facile activation (lower ideal shear strengths) of layer glide than calculated for the stoichiometric compound.
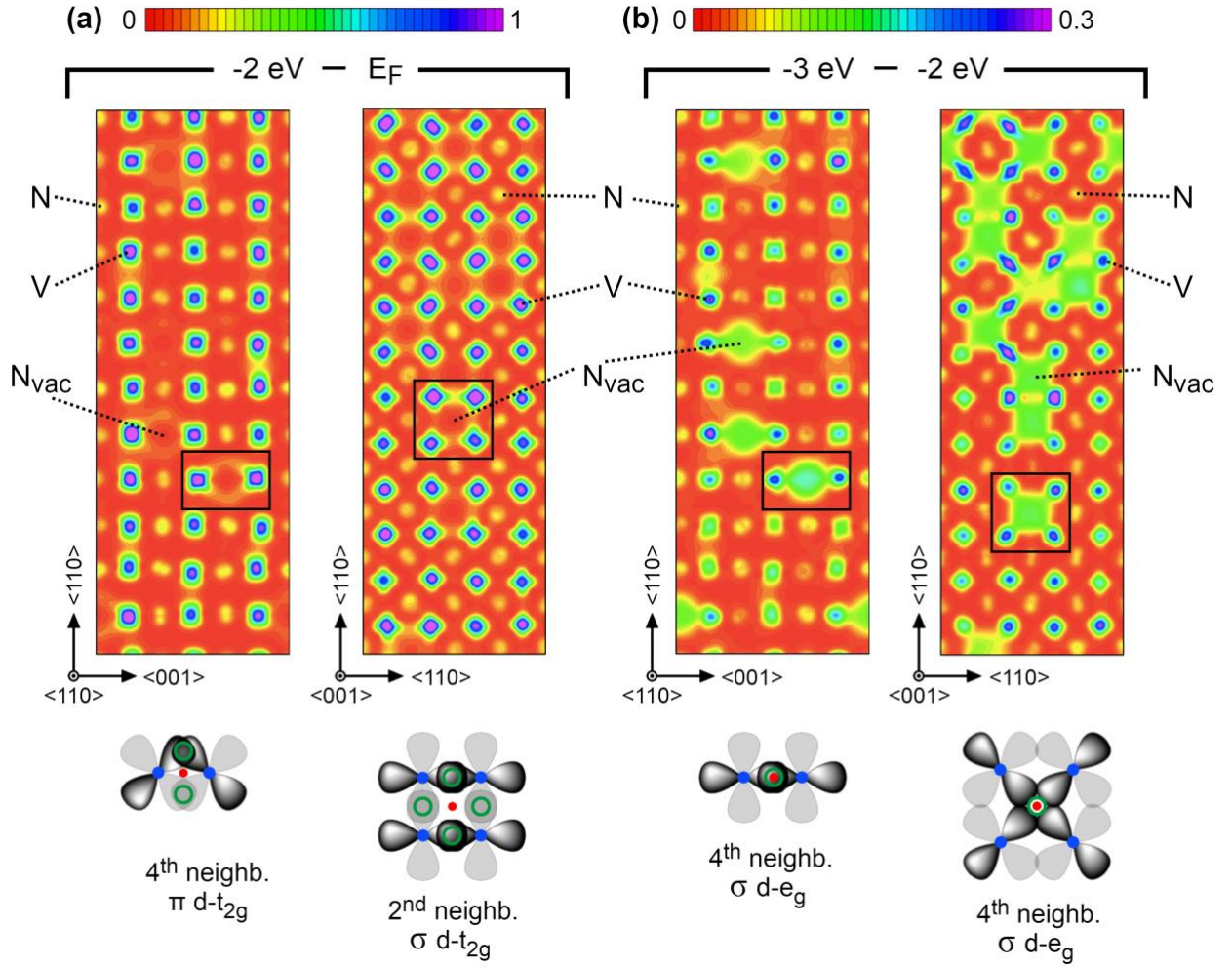
Fig. 7. Energy-resolved electron density maps of unstrained $VN_{0.8}$. The figure panels illustrate electronic states which primarily correspond to **(a)** d-t_{2g} [–2 eV - E_F] and **(b)** d-e_g [–3 - –2 eV] metallic bonds near the Fermi level E_F. Both panel **(a)** and **(b)** provide examples of electron density distributions on {110} and {001} crystallographic planes. The black squared frames facilitate visualization of different chemical bonds, which are also schematically represented by d-d orbital overlapping (see lower part of the figure). In illustrations at the bottom, blue and red dots mark V nuclei and anion-vacancy (N_{vac}) positions, respectively, whereas green circles indicate centers for constructive d-d electronic-wave interference. Note that, while **(a)** π and σ d-t_{2g} metallic bonding accumulate charge around the vacancy site, **(b)** σ d-e_g V – V bonding across vacancy sites yields electron accumulation on N_{vac}. The color scales are expressed in e–·Å–3.

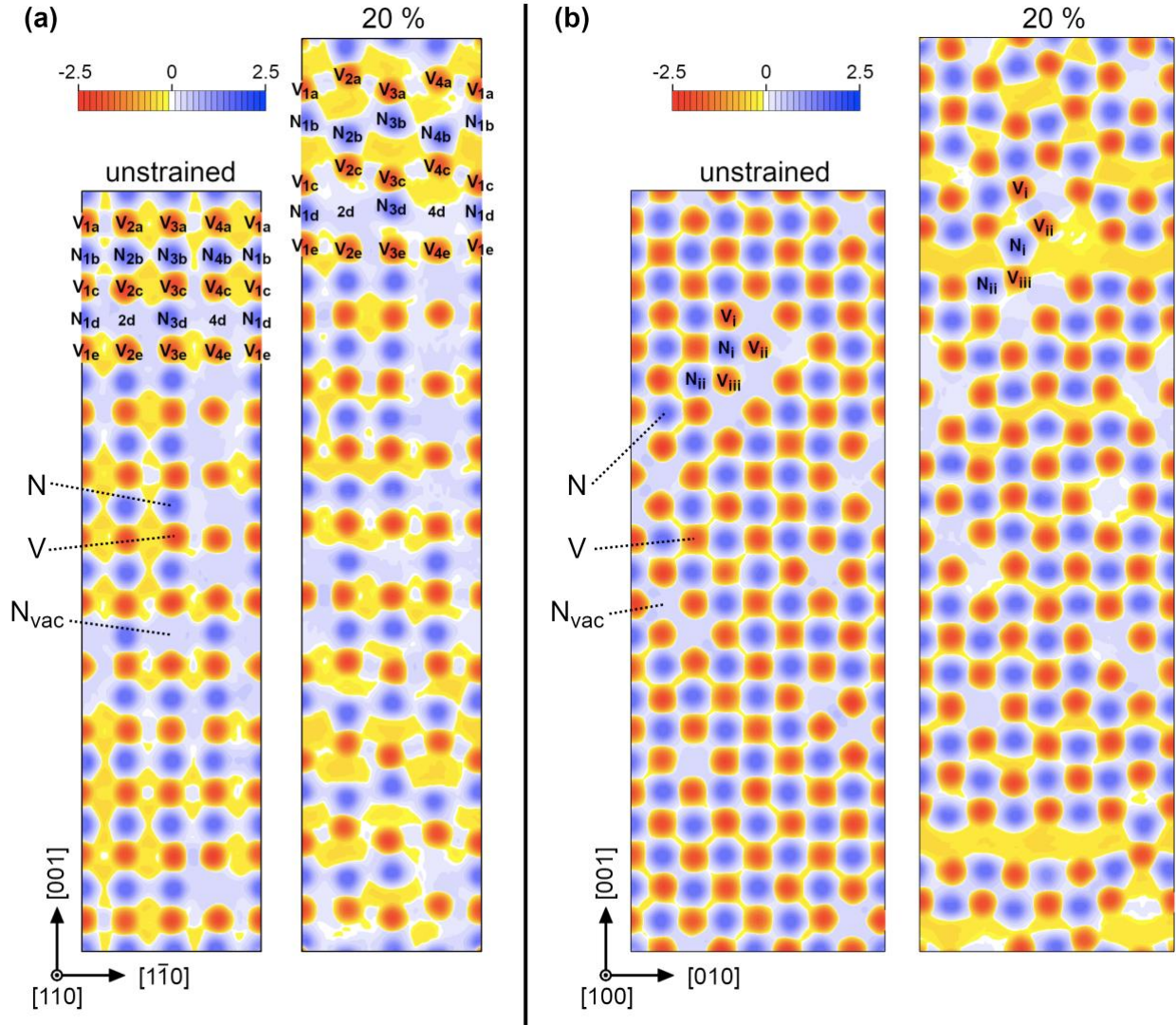**Fig. 8.** Electron transfer maps calculated for unstrained and 20% tensile-strained $VN_{0.8}(001)$ at 300 K. Examples of electron distributions are shown for **(a)** {110} and **(b)** {100} crystallographic planes parallel to the elongation direction. Electron accumulation (depletion) is indicated in blue (red-yellow) colors, with scale expressed in $e^-·Å^{-3}$.
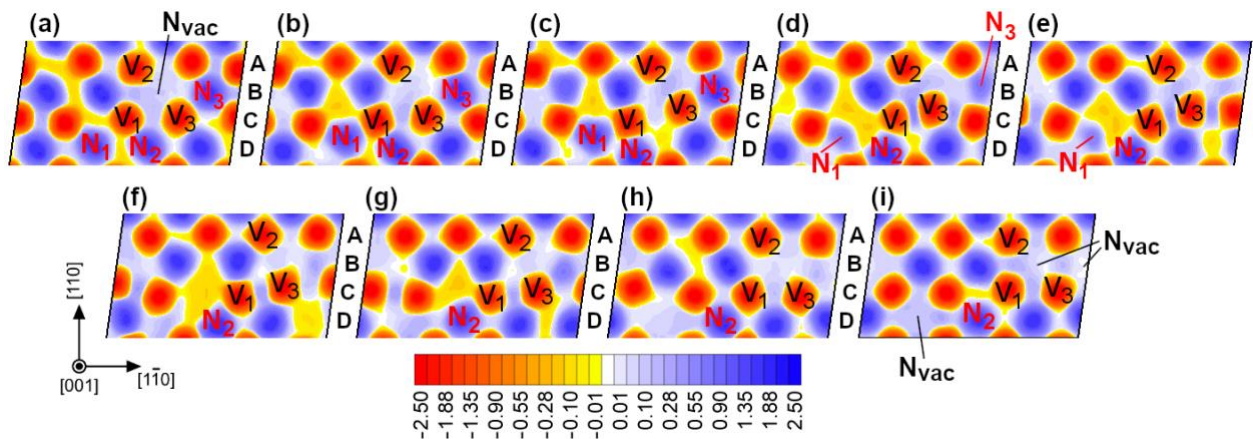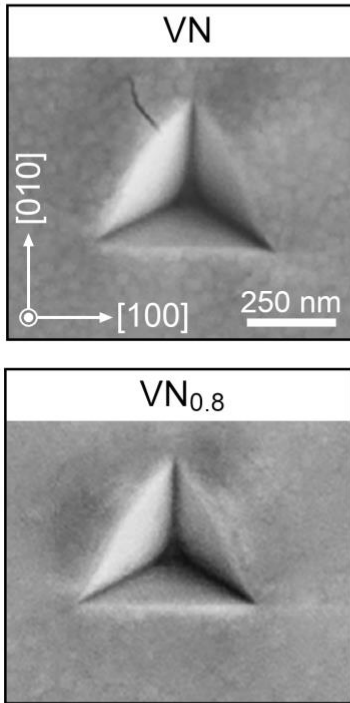

Fig. 9. Electron transfer maps calculated for a sequence of $VN_{0.8}(110)$ configurations during {110}⟨1$\bar{1}$0⟩ lattice slip (i.e., constant shear strain $\delta_{xz} = 14\%$, see **Fig. 6a**) at 300 K. Note that the figure shows only atomic layers near the glide-plane. The color scale is expressed in $e^-·Å^{-3}$.

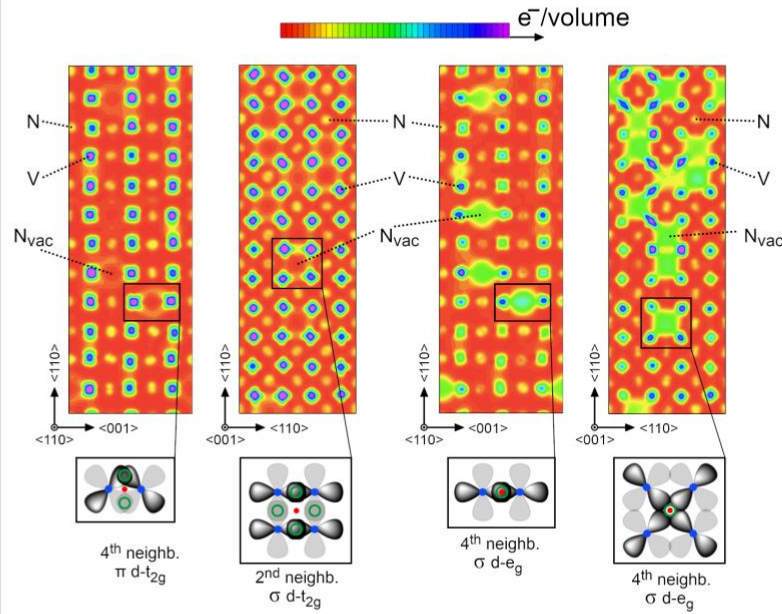# Increased hardness and toughness
in single-crystal B1 $VN_{0.8}$